Water Practice & Technology

IWA PUBLISHING

Water Practice & Technology Vol 18 No 10, 2315 doi: 10.2166/wpt.2023.152

Novel solar simulated photocatalytic heterolysis of pharmaceutical wastewater via slag nanocomposite immobilization: Optimization using response surface methodology

Kingsley Safo [a,*], Hussien Noby[a,b], Masatoshi Mitsuhara[c], Hiroshi Naragino[c] and Ahmed H. El-Shazly[a,d]

[a] Department of Chemical and Petrochemicals Engineering, Egypt-Japan University of Science and Technology, New Borg Al-Arab city, Alexandria, Egypt
[b] Materials Engineering and Design, Faculty Energy Engineering, Aswan University, Aswan, Egypt
[c] Interdisciplinary Graduate School of Engineering Science, Kyushu University, 6-1 Kasuga Koen, Kasuga, Fukuoka 816-8580, Japan
[d] Department of Chemical Engineering, Faculty of Engineering, Alexandria University, Alexandria, Egypt
*Corresponding author. E-mail: kingsley.safo@ejust.edu.eg

KS, 0000-0002-7491-3123

ABSTRACT

This study converted slag from the steelmaking industry into an Fe_2O_3-rich nanocomposite using solvothermal technique for photodegradation of pharmaceutical wastewater in an immobilized mode. The nanocomposite was characterized using XRF, SEM, EDX, TEM, FTIR, XRD, and UV–Vis spectrometer. The XRF analysis result reveals a significant increase in the weight percent of Fe_2O_3 and SiO_2, with a decrease in CaO content. The SEM images revealed the spherical and heterogeneous nature of the nanocomposite in shape and structure, while the FTIR confirms the increase in the vibration band of Si–O–Si and Fe–O with a reduction in the wide stretch mode of Ca–O. The XRD result illustrated the crystalline peak of Fe_2O_3 with a nanoparticle crystal size of 15.17 nm. The slag nanocomposite was used for the photodegradation of paracetamol. The optimum operating parameters were obtained using response surface methodology at an R^2 value of 0.99 and p-value < 0.05. The degradation efficiency obtained at the optimum value was 96.96%. The degradation efficiency of the fifth repeated cycle of the immobilized nanocomposite was 77.89%. The degradation mechanism revealed that OH• radical was the major species of the degradation process. This work showed that slag nanocomposite might be effectively used for pharmaceutical wastewater treatment.

Key words: nanocomposite, optimization analysis, pharmaceutical wastewater, photodegradation, response surface methodology, slag

HIGHLIGHTS

- Slag waste was converted into slag nanocomposite and full characterization was achieved.
- High photodegradation of paracetamol was attained.
- Degradation optimization was attained using response surface models.
- Immobilized nanocomposite achieved good stability and recyclability.
- Reactive oxidant species investigation was achieved.

GRAPHICAL ABSTRACT

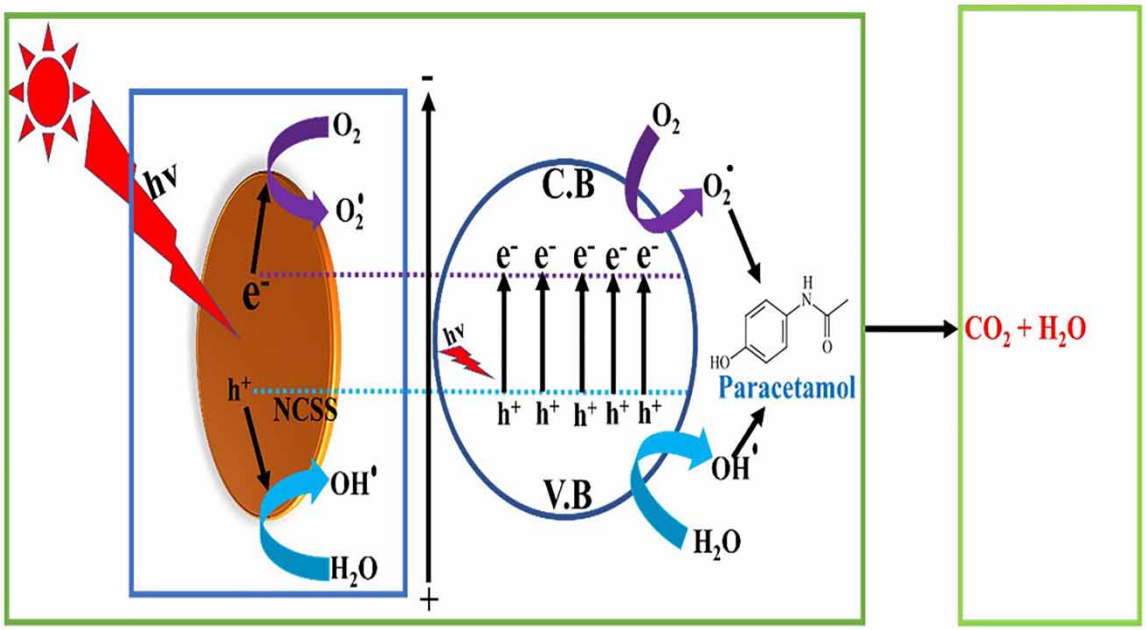

1. INTRODUCTION

The pharmaceutical sector has recently expanded due to the rising demand for its many goods, which are used to treat animals and humans (Alalm *et al.* 2015). Pharmaceutical industrial wastewater includes several bio-recalcitrant organics that are challenging for traditional wastewater treatment methods to eliminate (Gar Alalm *et al.* 2016). Not only do industries produce highly concentrated wastewater in medicines, but groundwater, surface water, and municipal wastewater have also been documented to contain small amounts of various pharmaceuticals (Shi *et al.* 2019). Due to their widespread use and intake in humans and animals, medicines and antibiotics are regarded as the most important pharmacological chemicals (Alalm *et al.* 2015; Shi *et al.* 2019). The pharmaceuticals are also widespread in the sewage and must be removed because of their possible negative effects on human health and ecosystems, like the following references clearly highlight (Di Marcantonio *et al.* 2021, 2023).

The steelmaking industry generates a huge quantity of byproducts (Kang *et al.* 2015). Slag is a solid byproduct produced during the steelmaking process (Proctor *et al.* 2000). The yearly global production of steel byproducts in the form of slag exceeds 50 million tons (Tsakiridis *et al.* 2008). SiO_2, Fe_2O_3, Al_2O_3, P_2O_5, CaO, MnO, MgO, and TiO_2 are the major constituents of steel slag (Tossavainen *et al.* 2007). The storage of this slag necessitates the use of a vast quantity of land and results in significant contamination of the environment (Wang *et al.* 2014; Safo *et al.* 2022a). Appropriate treatment and the use of this slag to reduce its pollution impact on the environment are becoming increasingly important.

A few recent researches have shown that transforming slag into a nanocomposite may boost the efficiency of the photodegradation reaction due to the enhanced dispersion of iron in water and the potential of iron reuse (Safo *et al.* 2022a, 2022b). Numerous water treatment applications have made use of steel slag that has been ground into a nanocomposite. However, there are limits to the amount that may be collected and reused (Mensah *et al.* 2022; Onen *et al.* 2023). In addition, the issue of collection may be resolved by coating the supporting plate with a catalyst. However, typical immobilization procedures such as heat bonding are energy-intensive (Khataee *et al.* 2009). Therefore, in this study, immobilization was done using Polysiloxane and aluminum plates without expending any energy. Polysiloxane may form strong bonds between the plates and catalyst particles (Samy *et al.* 2020). Moreover, acid treatment was used to convert the slag into a nanocomposite.

For the first time, steel waste was synthesized into nanocomposites steel slag (NCSS) using the solvothermal preparation technique and applied under a novel photo reactor for photodegradation of paracetamol (PC) in a reusable immobilize mode. The impacts of operational factors, such as catalyst dosage, pH, PC concentration (PC), and reaction time, were investigated through response surface methodology (RSM). The reusability of NCSS was also assessed to study the stability of the produced nanocomposite.

2. MATERIALS AND METHODS

In this investigation, slag from Egypt's Ezz steel was examined. Nitric acid (69% HNO_3), hydrochloric acid (37% HCl), and PC were purchased from the United Kingdom (Fisher Scientific Company).

The preparation of the nanocomposite steel slag (NCSS) was done based on our previous studies (Safo *et al.* 2022a). In brief, the steel slag was added to 10 mL of HNO_3 in a glass beaker and continuously stirred at 500 rpm at room temperature for 5 h. The solution was poured into a glass dish and dried at 70 °C for a day (24 h). The dry samples were mashed and calcined for 60 min at 1,000 °C. The final product was named nanocomposite steel slag (NCSS).

In addition, the coating was done using the method reported by Gar Alalm *et al.* (2018). In brief, the immobilization of the catalyst was done by coating the surface of a 3003-grade aluminum plate of thickness 2 mm and diameter 60 mm containing 1 mm thickness of polysiloxane with the optimum amount of NCSS from the RSM. The plate was then dried at room temperature for 720 min. Finally, the plate was washed with distilled water for several times to remove unbonded particles and to validate the tight connection between the aluminum plates and the nanocomposite.

2.1. Characterization techniques

The composition, including the chemical and elemental components of the prepared samples, was characterized by energy-dispersive X-ray spectroscopy (JEOL, JEM-2100F, Japan) and X-ray fluorescence (Shimadzu XRF, Japan). The prepared sample's microstructure, morphology, and nanostructure were analyzed using a scanning electron microscope (SEM) (JEOL JSM-6010LV SEM, Japan). Transmission electron microscope (TEM) was used to obtain high-resolution images. The bond and the functional groups of samples were also examined using Fourier Transform Infrared Spectrometer (Shimadzu FTIR-8400s, Japan). The crystallographic information of the raw slag and NCSS were also examined using X-ray diffraction with a 1.54 Å, Cu-Kα radiation beam (Shimadzu XRD-6100, Japan).

2.2. Experimental apparatus and procedure

The test was done based on the matrix parameters from the RSM, as shown in Table 1, at varying pH from 3 to 12 and PC concentrations of 10–30 ppm under the novel photo rector.

Table 1 | Factors and their matrix input variables in BBD

Factors			Levels		
Name	Unit	Label	Lowest value −1	Median value 0	Highest value +1
NCSS dose	mg/L	A	10	35	60
PC	ppm	B	10	20	30
Time	minute	C	10	35	60

The photo reaction activity was illuminated with a novel solar reactor made up of a metal halide lamp (Philips) of photo flux 220 Wcm^2, a wavelength of 510 nm, and a power of 400 W placed 15 cm above the solution surface as shown in Figure 1.

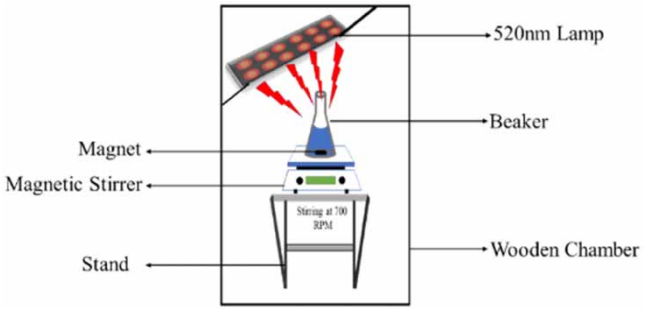

Figure 1 | Solar novel photo reactor.

Using high-performance liquid chromatography (HPLC), the PC was measured for the initial and final degradation processess after the samples were filtered using a syringe filter of porosity 0.2 um into a C-18 column. As a mobile phase, a combination of ultrapure water and methanol with corresponding proportions of (60:40) was utilized to detect the signal peak of the PC. The injection process was done at a flow rate of 0.9 ml/min, 40 °C temperature, and 25 ml volume.

The degradation efficiency (η) was then calculated using the following equation (Safo *et al.* 2023):

$$\eta = (\Delta C)/C_0 \times 100 \quad (1)$$

Here, C_0 signifies the concentration at a zero time, and ΔC is the difference between the initial concentration and the concentration at any given time, t.

2.3. Experimental design

The optimization of operational parameters such as A; NCSS dosage, B; PC, and C; reaction time, was done using RSM. As shown in Table 1, the response matrix was generated using a Box–Behnken design (BBD). The BBD was used because it does not need models where all factors are simultaneously performed at their maximum or minimum values but rather gives the same information as a complete factorial design with fewer experiments (Safo *et al.* 2023). Consequently, this approach is advantageous for avoiding trials under severe circumstances that might provide unsatisfactory findings (Tetteh *et al.* 2021).

3. RESULT AND DISCUSSION

3.1. Characterization of the prepared nanocomposite

3.1.1. XRF and FTIR analysis

Figure 2(a) displays the XRF analysis of the obtained nanocomposite. Raw-slag mostly consists of iron oxides (35.5%), calcium oxides (45.5%), silica (9.09%), and a small amount of titanium dioxide (0.446%) with a loss on ignition (LOI) of 1.824% of the total weight of the slag. After the raw-slag was treated with HNO_3, the slag produced a higher concentration of Fe_2O_3 and SiO_2 by weight, whereas a lower concentration of CaO was produced as shown in Figure 2(a) of the NCSS. Moreover, the variations in vibrating peaks for raw-slag and the prepared NCSS were tracked using Fourier transform infrared spectrometer (FTIR) spectra (spectral ranging from 500 to 4,000 cm^{-1}).

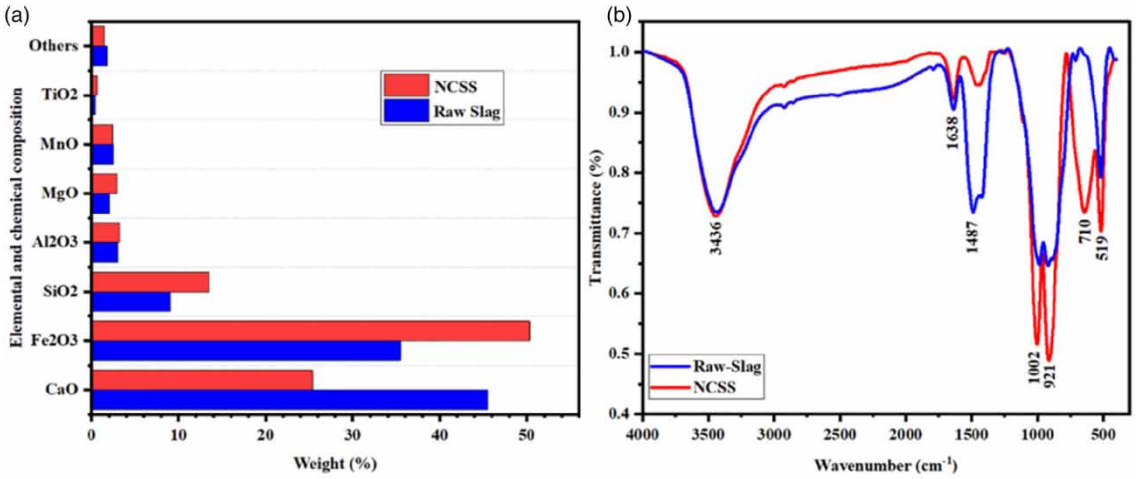

Figure 2 | (a) XRF and (b) FTIR plot of NCSS.

It also emerged in the raw-slag for both the stretching vibration of the O–H peak at 3,436 cm^{-1} and the bending vibration of the H–O–H absorption peak at 1,638 cm^{-1}, as shown in Figure 2(b). The former and the latter might be associated with chemically bonded water (Bai *et al.* 2018). These showed that crystallization and adsorption water were present in the raw-slag, and the same occurrences were seen in the NCSS nanocomposite produced, as shown in Figure 2(b). Furthermore, there was a distinctive absorption peak of about 1,487 cm^{-1} whose

intensity was reduced, and a certain displacement occurred. This might be ascribed to the raw-slag chemical and physical interaction with the HNO_3 and the heat treatment as described in a previous study (Safo *et al.* 2023) which diminished the raw-slag lattice deformation and vibration, reducing the corresponding stretching vibration C–O modes, which generally arise if a sample increases in CaO content (Ma *et al.* 2019; Jeon *et al.* 2021). Additionally, the absorption peak of 1,002 and 710 cm^{-1} are features of Si–O and Si–O–Al stretching modes whose vibration stretch increases, indicating an increase in silica and silicate content (Bai *et al.* 2018; Sanad *et al.* 2021). The bond around 519 cm^{-1} is a vibration of Fe–O, Mg–O, Ti–O, and other metal-oxides (Sarkar *et al.* 2019).

3.1.2. SEM and EDX analysis

Figure 3(a) and 3(b) shows SEM and energy-dispersive X-ray (EDX) images of the nanocomposite steel slag (NCSS) analyzed using FE-SEM. This was done to examine the surface morphology of the prepared NCSS catalyst sample. As shown in Figure 3(a), at 2,000 magnifications, the findings indicate that the NCSS has a spherical and heterogeneous form and structure. Wide macropores and connected grains may also be seen in the SEM image.

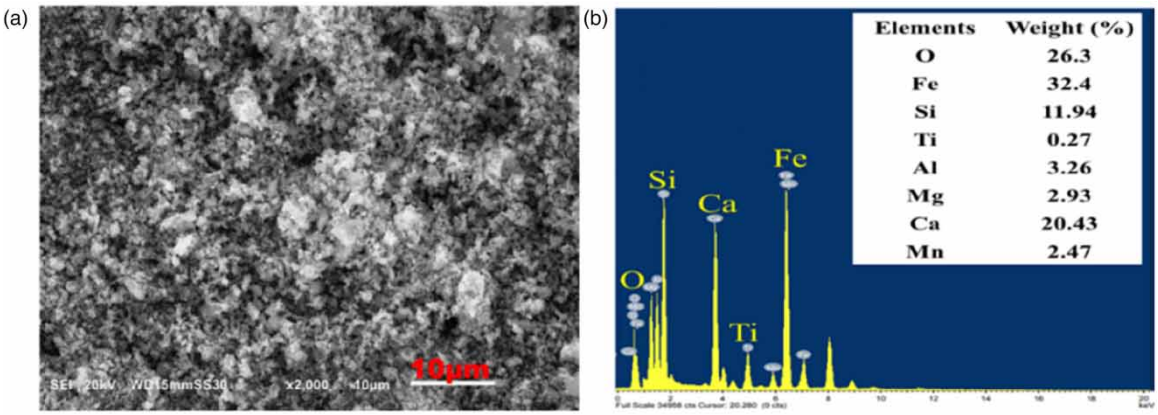

Figure 3 | (a) SEM and (b) EDX images of NCSS.

The EdX analysis of the NCSS as shown in Figure 3(b) reveals that the NCSS contains around 26.3 wt% of O, 32.4 wt% of Fe, 11.94 wt% of Si, 0.27 wt% of Ti, 3.26 wt% of Al, 2.93 wt% of Mg, 20.43 wt% of Ca, and 2.47 wt% of Mn.

3.1.3. TEM and XRD analysis of the samples

The TEM image of the NCSS demonstrates that the NCSS contains a significant amount of unoxidized iron and silicon particles in the form of tiny, dark-shadowed particles as shown in Figure 4(a) (Cui *et al.* 2016).

The samples' X-ray diffraction patterns were examined using the Hanawalt System for Joint Committee for Powder Diffraction Standards (JCPDS). Figure 4(b) illustrates the XRD patterns of the raw-slag and the prepared NCSS which show the complex composition of raw-slag, which is made up of Hematite (Fe_2O_3, PDF No. 00-024-0072), Larnite (Ca_2SiO_4, PDF No. 00-006-0476), Calcite ($CaCO_3$ PDF No.00-003-0569), Laihunite ($Fe_{1.5}O_4Si$, PDF No. 01-078-1435), Esseneite ($AlCaFeO_6Si$ PDF No. 00-040-0496) and Andradite ($Ca_3Fe_2O_{12}Si_3$, PDF No. 00-003-1136. In the NCSS the crystallization diffraction peak centered at 2Θ of 47° for the Calcite ($CaCO_3$ PDF No.00-003-0569) vanished with an increase in the Hematite (Fe_2O_3, PDF No. 00-024-0072) peak at 35.56°. Indicating some degree of physical and chemical interaction between the raw-slag and HNO_3, as well as a lattice change in crystallinity after heat treatment at 1,000 °C. As a result, the bonding strength of raw-slag was increased, which corresponds with the FTIR and EDX results (Ali *et al.* 2020; Safo *et al.* 2022a).

3.2. Application of the novel catalyst for pharmaceutical wastewater treatment

The photocatalytic activity of the prepared samples NCSS was determined for the degradation of PC at immobilized NCSS dosage of 70 mg/L, PC concentration of 10 ppm and a varying pH from 3 to 12 as shown in Figure 5. First and foremost, a PC solution without an NCSS catalyst was recirculated under UV light for 60 min, and the results were recorded.

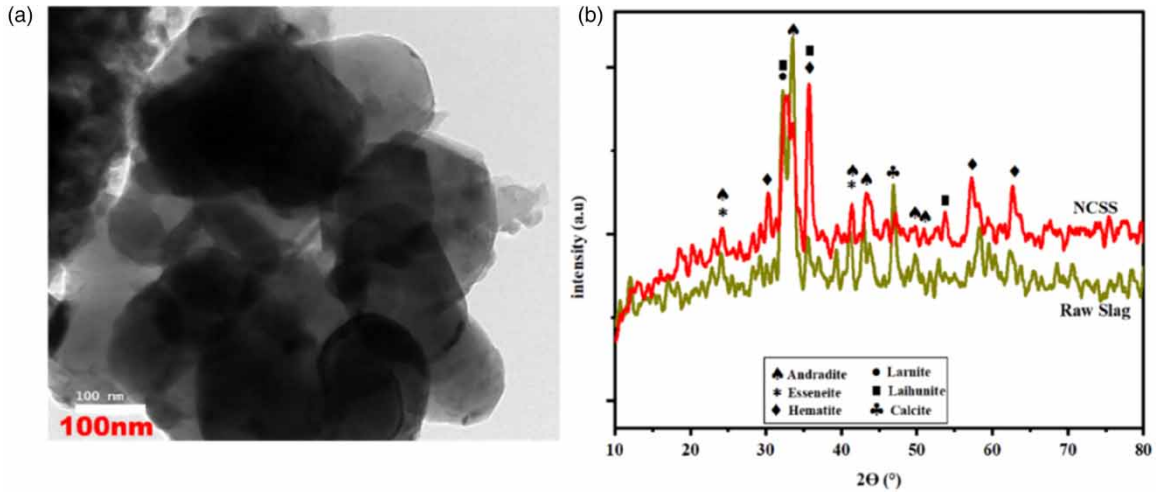

Figure 4 | (a) TEM images and (b) XRD plot of NCSS.

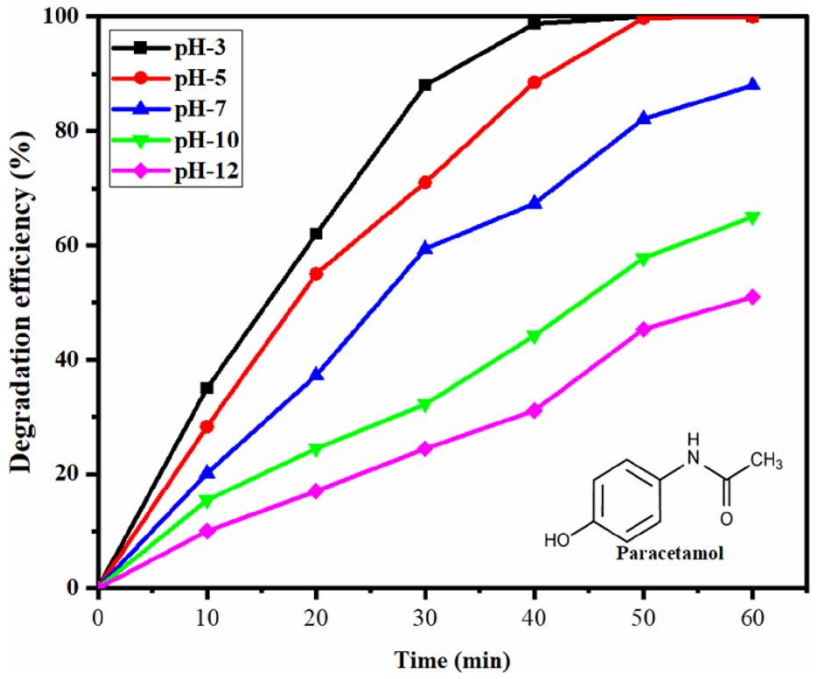

Figure 5 | PC photodegradation at different pH (conditions: NCSS dosage of 70 mg/L, PC concentration of 10 ppm, and time from 10 to 60 min).

The concentration of PC remained constant throughout the time, demonstrating that PC is non-degradable under visible light without a catalyst (Feng *et al.* 2013). The result in Figure 5 shows the degradation ability of NCSS over a time range of 10–60 min at different pH. The degradation was very low at the lower time of 10 but kept rising from 10 to 60 min time interval. This can be attributed to the transfer of photons from the light to the active site of the NCSS, which was very slow at the initial time, but as the time increased, more photons were transferred to the NCSS surface, which generated an electron hole capable of undergoing a redox reaction to breakdown the structure of the molecules of PC (Zia & Riaz 2020). Moreover, Figure 5 also shows that the photodegradation efficiencies of PC were 24.5, 41.2, 68.3, 89.2, and 97.92% at a pH of 12, 10, 7, 5, and 3, respectively, at a time of 40 min. The difference in the photodegradation efficiency at varying pH is associated with the nature of the protonation and deprotonation of the NCSS catalyst and PC molecules in a solution. At a pH of 3,

the surface of NCSS is positively charged, which adsorbs and degrades more of PC (Alalm *et al.* 2015). Moreover, at high pH, there is oxidation of the ions in the hematite content into iron hydroxides, which act as a scavenger for hydroxyl radicals which prevent the degradation of the molecules of PC (Yang *et al.* 2009).

It has been discovered that PC photodegradation using NCSS is equivalent to the performance of other catalysts previously utilized in photocatalytic degradation reactions. For instance, after 60 min of using Ag/Ag_2O-PTh catalyst, the highest degradation of PC was 98% (Zia & Riaz 2020). In another work, the photodegradation efficiency of PC after 3.5 h of oxidation using TiO_2/cellulosic fiber was only 90% (Yanyan *et al.* 2017). Moreover, the PC photodegradation achieved by Au/TiO_2 composites at 180 min was 68.8% (Nasr *et al.* 2019). In addition, the highest PC photodegradation achieved by TiO_2-graphite composite after 180 min was 88% (Vaiano *et al.* 2018).

3.3. Experimental design and data analysis

The results of 17 separate experiments are shown in Table 2, together with the photodegradation efficiencies of PC obtained from the actual experimental work and the predicted photodegradation efficiencies by the model at a pH of 3. The link between the operating parameters and the photodegradation efficiencies of PC is described in the following equation:

Table 2 | BBD matrix result of PC photodegradation efficiencies (%) at a pH of 3

	Actual value of operation parameters			Degradation efficiency		
Run order	NCSS (mg/L)	PC (ppm)	Time (min)	Actual value	Predicted value	Residual
1	35	20	35	73.92	75.00	−1.03
2	35	20	35	74.50	75.00	−0.50
3	10	30	35	30.00	29.87	0.12
4	10	20	10	17.00	15.25	1.75
5	35	30	10	42.00	43.87	−1.87
6	35	20	35	76.50	75.00	1.50
7	10	20	60	49.00	51.00	−2.00
8	35	30	60	77.00	75.13	1.87
9	60	10	35	78.00	78.12	−0.13
10	35	10	10	46.00	47.87	−1.87
11	60	20	10	51.00	49.00	2.00
12	35	20	35	73.50	75.00	−1.50
13	60	20	60	89.00	90.75	−1.75
14	35	20	35	75.50	75.00	0.50
15	35	10	60	96.00	94.13	1.87
16	10	10	35	46.00	45.87	0.13
17	60	30	35	71.00	71.12	−0.12

$$Y(\%) = -23.67000 + 2.29100A + 0.635000B + 1.80300C + 0.009000AB + 0.002400AC - 0.015000BC - 0.026000A^2 - 0.025000B^2 - 0.011600C^2 \quad (2)$$

where Y (%) is the photodegradation efficiency (%) of PC at a pH of 3, A is the NCSS catalyst dosage, B is the PC, and C is time in minutes.

The high values of R^2 (98.58%) and adjusted R^2 (95.39%), as well as the standard deviation of 2.13 and the little discrepancy between predicted and actual PC photodegradation efficiency at a pH of 3, provide evidence that the model was suitable for the application, as shown in Table 3.

In order to determine whether or not the model is significant, an ANOVA test for PC photodegradation efficiency was carried out, and the results are shown in Table 4. According to the *F*-values and *p*-values, the NCSS catalyst dosage and the irradiation time had a more substantial impact on the photodegradation efficiency

Table 3 | ANOVA of the fit statistic results for the response *Y* (%) quadratic models

Std. Dev.	2.18	R^2	0.9956
Mean	62.76	Adjusted R^2	0.9899
C.V. %	3.47	Predicted R^2	0.9390
		Adeq precision	47.1864

Table 4 | ANOVA report for the photodegradation efficiencies of PC at a pH of 3

Source	Sum of squares	df	Mean square	*F*-value	*p*-value
Model	7,504.81	9	833.87	175.55	<0.0001
A-NCSS	2,701.13	1	2,701.13	568.66	<0.0001
B-PC	264.50	1	264.50	55.68	0.0001
C-Time	3,003.13	1	3,003.13	632.24	<0.0001
AB	20.25	1	20.25	4.26	0.0778
AC	9.00	1	9.00	1.89	0.2111
BC	56.25	1	56.25	11.84	0.0108
A^2	1,111.84	1	1,111.84	234.07	<0.0001
B^2	26.32	1	26.32	5.54	0.0508
C^2	221.32	1	221.32	46.59	0.0002
Residual	33.25	7	4.75		
Pure error	5.00	4	1.25		
Cor total	7,538.06	16			

of PC, while the PC had the least influence. Moreover, the low *P*-value indicates the significance of the prediction model.

3.3.1. Influence of operating conditions

The influence of operational conditions on PC photodegradation efficiency was shown by the 3D and contour plots in Figure 6. The increase in NCSS catalyst dosage improves PC photodegradation efficiency by increasing the number of active sites that may adsorb photons and create reactive species (Zia & Riaz 2020). However, applying a catalyst dosage greater than the optimal (48.96 m g/L Figure 7) reduces the effectiveness of the photodegradation owing to the scattering effect, as shown in Figure 6(a). This is due to the rise in solution turbidity, which is a result of the high catalyst dosage reducing the number of photons excited by the catalyst's active sites. Turbidity arises from the presence of suspended or dissolved particles in water, which disperse light and result in the visual manifestation of cloudiness or murkiness in the water (Zia & Riaz 2020; Safo & Berko 2023). Furthermore, at high catalyst dosages, nanoparticle aggregation rises, reducing the surface area accessible for photon adsorption (Villota *et al.* 2016).

According to the findings in Figure 6(b), a rise in the PC at the beginning of the experiment had an adverse effect on the amount of PC that was successfully degraded. The increased number of PC molecules that get adsorbed on the surface of NCSS in the presence of increasing concentrations of PC causes a reduction in the number of active sites, which in turn causes a drop in the photodegradation efficiency (Alalm *et al.* 2015). The reaction interaction effect between NCSS dosage and PC can be further described according to the analysis of variance in Table 4. There was a significant relationship between NCSS dosage and PC. This relationship is also depicted in the plot of 3D and contour in Figure 6(c), where increasing NCSS dosage increased degradation efficiency at low PC concentrations.

A numerical optimization study was conducted where the optimum operating values were 56.395 min, 48.96 mg/L, and 10.76 ppm for irradiation time, NCSS catalyst dosage, and PC, respectively, as shown in Figure 7 with a photodegradation efficiency of 96.96%.

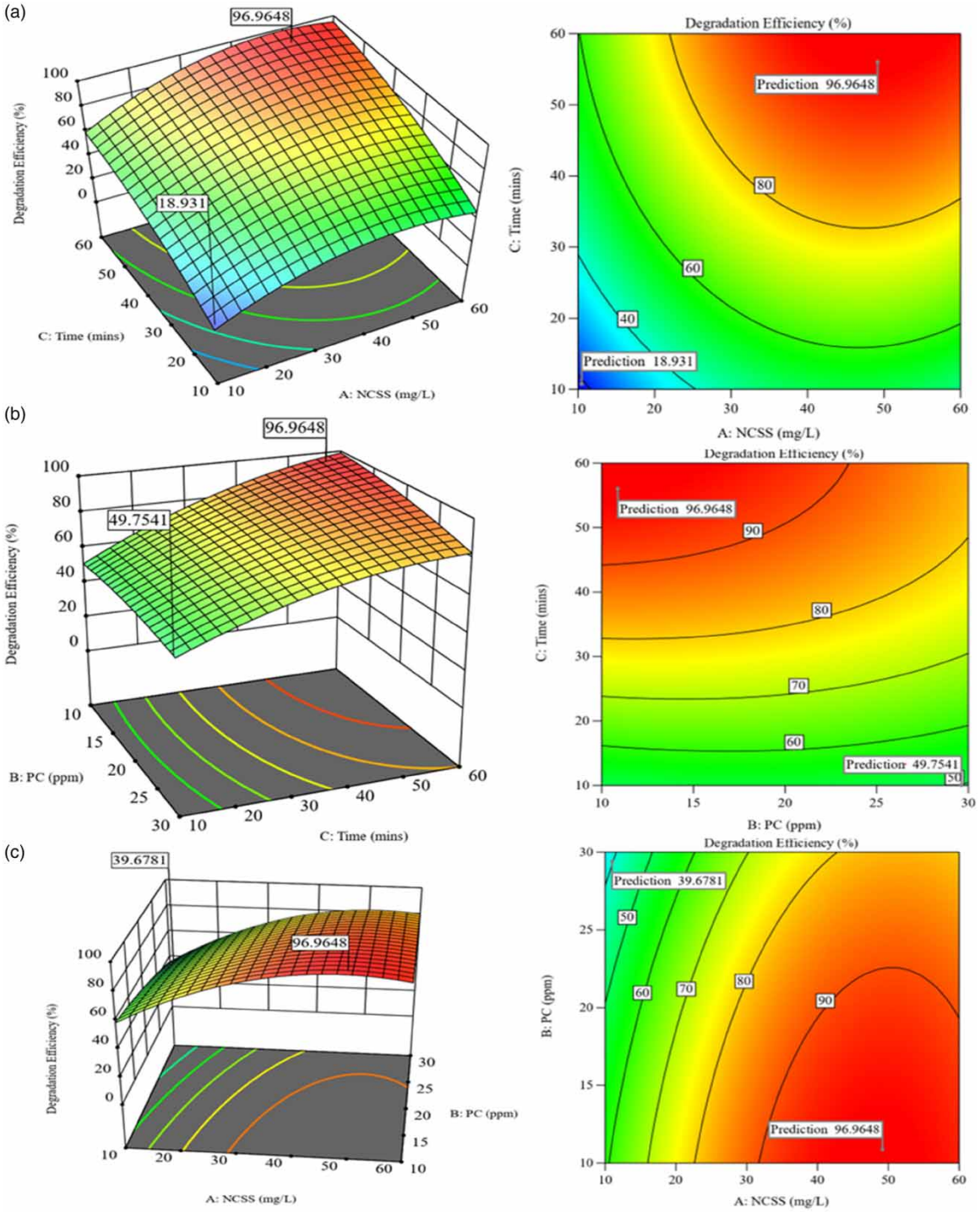

Figure 6 | 3D and contour plot of effect: (a) NCSS dosage and time, (b) PC and time, (c) NCSS dosage and PC.

3.4. Degradation mechanism

The mechanism of PC photodegradation using the NCSS catalyst is shown in Figure 8, along with the radicals produced on the NCSS catalyst during the photocatalytic reaction. After the excitation of the NCSS catalyst by a light source whose energy was greater than the energy of the bandgap, electrons in the valence band (VB) become excited and begin to move from the VB to the conduction band (CB) creating holes (h^+) in the VB and free electrons (e^-) in the CB as depicted in the following equation:

$$hv + \text{NCSS} \rightarrow \text{VB}h^+ + \text{CB}e^- \quad (3)$$

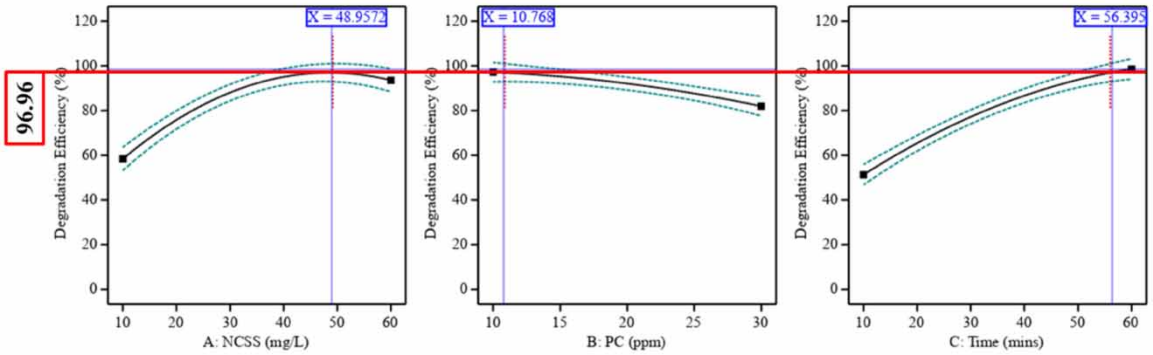

Figure 7 | Optimum operating parameters for PC photodegradation at a pH of 3.

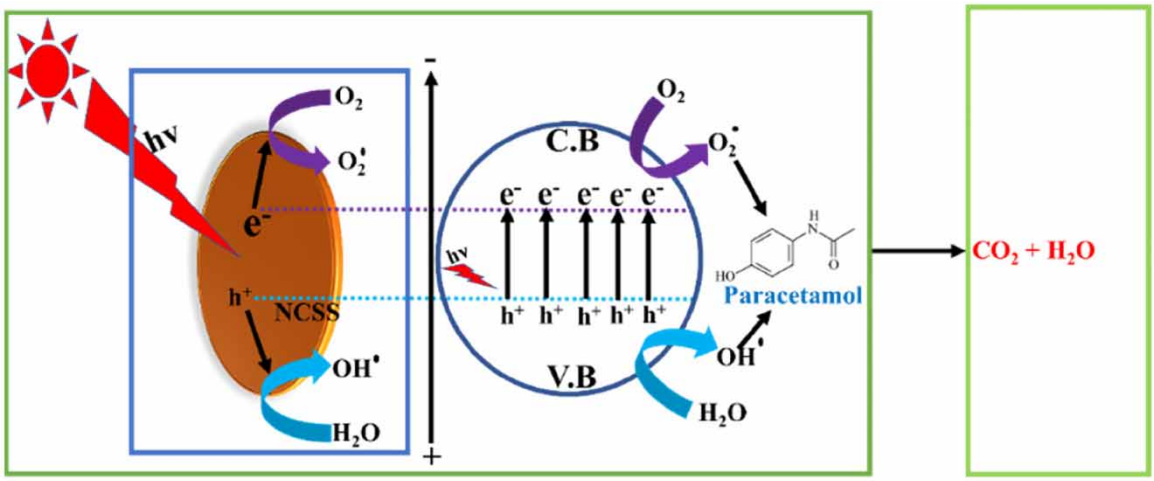

Figure 8 | The mechanism of PC photodegradation reaction using NCSS catalyst.

The hole in the VB undergoes an oxidation reaction with moisture, water, and hydroxyl ions to produce hydroxyl free radicals ($OH\bullet$), as described in the following equation:

$$h^+ + H_2O \rightarrow H^+ + OH\bullet \quad (4)$$

Any PC molecule that is adsorbed on or near the NCSS catalyst active surface is attacked by the hydroxyl radicals into a non-harmful compound, as illustrated in Equation (5) and demonstrated in a previous study (Chacón *et al.* 2022):

$$OH\bullet + \text{PC molecules} \rightarrow CO_2 + H_2O \quad (5)$$

Additionally, the free electron in the CB undergoes a reduction reaction with dissolved oxygen to create superoxide radicals ($O_2\bullet$), as demonstrated in the following equation:

$$e^- + O_2 \rightarrow O_2\bullet \quad (6)$$

which also attach these PC molecules to non-harmful compounds such as H_2O and CO_2, as depicted in Figure 6 and in the following equation:

$$O_2\bullet + \text{PC molecules} \rightarrow CO_2 + H_2O \quad (7)$$

By continuously producing OH• and O_2• radicals to undergo oxidation reactions with PC molecules, there will be a complete convention of transformation products into CO_2 and H_2O.

To determine how O_2• radicals, OH• radicals and holes (h^+) contributed to the photocatalytic degradation process, 1 mM isopropanol (ISOP), ammonium oxalate (AMO) and benzoquinone (BZQ) (Xu *et al.* 2019) were utilized as scavengers, respectively. The impact of the scavenger's effect on PC photodegradation using 50 mg/L NCSS catalyst is shown in Figure 9 at a pH of 3 and a PC concentration of 10 ppm. The addition of ISOP, AMO, and BZQ lowered the photodegradation efficiency to 42.45, 77.32, and 71.91%, respectively, whereas in the absence of scavengers, the efficiency was 97.59%. The results showed that the PC photodegradation effectiveness was influenced by O_2• radicals, OH• radicals and holes (h^+). However, compared to other radicals, OH• radicals contributed more significantly to the photocatalytic degradation of PC molecules.

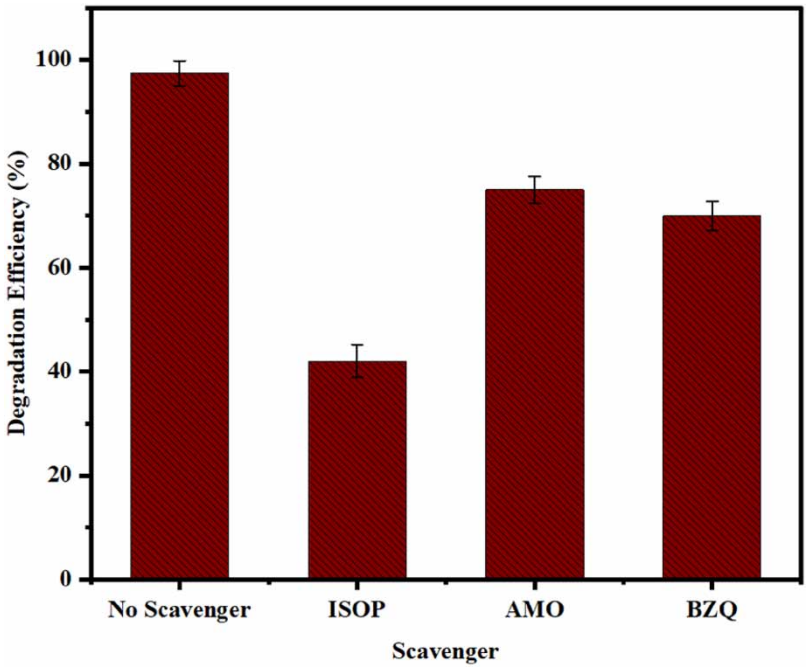

Figure 9 | Scavengers' effect on PC photodegradation under trapping experiments (conditions: NCSS dosage of 50 mg/L, pH of 3, PC concentration of 10 ppm and time of 60 min).

3.5. Reusability of immobilized NCSS

The photodegradation efficiency of PC utilizing immobilized NCSS catalysts was examined, as demonstrated in Figure 10. Five consecutive repeating cycles of the degradation process at an NCSS dosage of 50 mg/L, pH of 3, and PC concentration of 10 ppm were used to evaluate the reusability and industrial application of the catalyst.

The photodegradation efficiencies of the repeating cycle were 96.23, 94.13, 92.78, 89.33, and 87.24%, respectively. The minor reduction in photodegradation efficiencies in subsequent runs was caused by the restricted amount of particles exiting the plate due to the magnet's quick movement. Furthermore, in each run, the PC molecules may cover the active sites of the coated NCSS catalyst particles. The reduction in active sites led to a drop in the photodegradation efficiency in the last two repeating cycles. However, the high photodegradation efficiencies in the five repeating cycles confirm the stability and reusability of the NCSS catalyst for both coated and suspended modes, making it a viable catalyst for industrial wastewater treatment.

4. CONCLUSION

In this work, a raw waste slag was synthesized successfully and utilized for the photodegradation of PC in an immobilized mode. The characterization of raw-slag and the produced NCSS catalyst demonstrated that the produced catalyst is stable and can function as a nanocomposite with different crystalline peaks. NCSS achieved

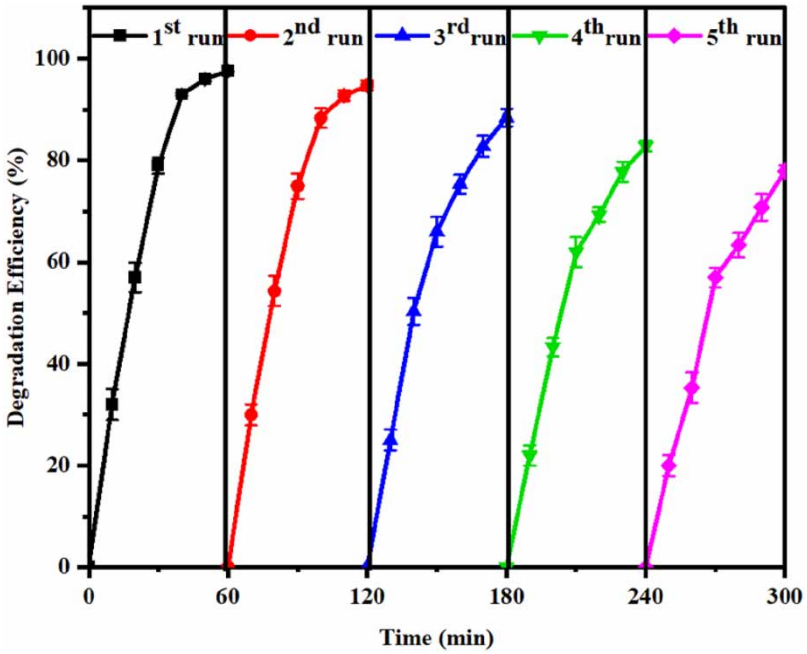

Figure 10 | The reusability performance of immobilized NCSS (conditions: NCSS dosage of 50 mg/L, pH of 3, and PC concentration of 10 ppm).

complete degradation of PC molecules after 60 min at a pH of 3. The photodegradation was optimized using RSM, resulting in 96.96% degradation efficiency at a pH of 3, an NCSS dosage of 48.96 mg/L, PC concentration of 10.77 ppm, and a time of 56.4 min. Hydroxyl free radicals were observed to be the most deriving reactive oxidation species for the degradation process. The PC degradation efficiency in five repeating cycles at the optimum parameters were 96.23, 94.13, 92.78, 89.33, and 87.24%, respectively. This result indicates that the final effluent of the pharmaceutical wastewater could be treated with an NCSS catalyst produced from slag waste before discharge into water bodies to reduce the risk posed to humans and the environment.

ACKNOWLEDGEMENTS

The authors want to express their appreciation to the Japan International Cooperation Agency (JICA) and Egypt-Japan University of Science and Technology (E-JUST) for providing financial and technical support, respectively. Additionally, the first author, K.S., wishes to thank TICAD 7 for the scholarship opportunity for the master's in chemical and Petrochemical Engineering and also the support of Mavis Berko, Elsa Odira and Abigail Oteng.

AUTHOR CONTRIBUTIONS

K. S. conceptualized the whole article, developed the methodology, validated the article, conducted a formal analysis, investigated the article, rendered support in data curation, wrote the original draft, wrote the-review and edited the article. H. N. conceptualized the article, rendered support in data curation, wrote the review and edited the article, and supervised the work. M. M. rendered support in data curation, wrote the review and edited the article, and supervised the work. H. N. rendered support in data curation, wrote the review and edited the article, and supervised the work. A. H. E. rendered support in data curation, wrote the review and edited the article, and supervised the work.

DATA AVAILABILITY STATEMENT

All relevant data are included in the paper or its Supplementary Information.

CONFLICT OF INTEREST

The authors declare there is no conflict.

REFERENCES

Alalm, M. G., Tawfik, A. & Ookawara, S. 2015 Degradation of four pharmaceuticals by solar photo-Fenton process: Kinetics and costs estimation. *J. Environ. Chem. Eng.* **3**, 46–51. https://doi.org/10.1016/j.jece.2014.12.009.

Ali, A. S., Khan, I., Zhang, B., Nomura, K., Homonnay, Z., Kuzmann, E., Scrimshire, A., Bingham, P. A., Krehula, S., Musić, S., Akiyama, K. & Kubuki, S. 2020 Photo-Fenton degradation of methylene blue using hematite-enriched slag under visible light. *J. Radioanal. Nucl. Chem.* **325**, 537–549. https://doi.org/10.1007/s10967-020-07238-x.

Bai, T., Song, Z. G., Wu, Y. G., Hu, X. D. & Bai, H. 2018 Influence of steel slag on the mechanical properties and curing time of metakaolin geopolymer. *Ceram. Int.* **44**, 15706–15713. https://doi.org/10.1016/j.ceramint.2018.05.243.

Chacón, F. J., Cayuela, M. L. & Sánchez-Monedero, M. A. 2022 Paracetamol degradation pathways in soil after biochar addition. *Environ. Pollut.* **307**. https://doi.org/10.1016/j.envpol.2022.119546.

Cui, Y., Liu, S., Smith, K., Yu, K., Hu, H., Jiang, W. & Li, Y. 2016 Characterization of corrosion scale formed on stainless steel delivery pipe for reclaimed water treatment. *Water Res.* **88**, 816–825. https://doi.org/10.1016/j.watres.2015.11.021.

Di Marcantonio, C., Chiavola, A., Paderi, S., Gioia, V., Mancini, M., Calchetti, T., Frugis, A., Leoni, S., Cecchini, G., Spizzirri, M. & Boni, M. R. 2021 Evaluation of removal of illicit drugs, pharmaceuticals and caffeine in a wastewater reclamation plant and related health risk for non-potable applications. *Process Saf. Environ. Prot.* **152**, 391–403. https://doi.org/10.1016/j.psep.2021.06.024.

Di Marcantonio, C., Chiavola, A., Gioia, V., Leoni, S., Cecchini, G., Frugis, A., Ceci, C., Spizzirri, M. & Boni, M. R. 2023 A step forward on site-specific environmental risk assessment and insight into the main influencing factors of CECs removal from wastewater. *J. Environ. Manage.* **325**, 116541. https://doi.org/10.1016/j.jenvman.2022.116541.

Feng, X., Zhang, Q., Cong, P. & Zhu, Z. 2013 Determination of the paracetamol degradation process with online UV spectroscopic and multivariate curve resolution-alternating least squares methods: Comparative validation by HPLC. *Anal. Methods* **5**, 5286–5293. https://doi.org/10.1039/c3ay40747k.

Gar Alalm, M., Tawfik, A. & Ookawara, S. 2016 Solar photocatalytic degradation of phenol by TiO_2/AC prepared by temperature impregnation method. *Desalin. Water Treat.* **57**, 835–844. https://doi.org/10.1080/19443994.2014.969319.

Gar Alalm, M., Samy, M., Ookawara, S. & Ohno, T. 2018 Immobilization of S-TiO_2 on reusable aluminum plates by polysiloxane for photocatalytic degradation of 2,4-dichlorophenol in water. *J. Water Process Eng.* **26**, 329–335. https://doi.org/10.1016/j.jwpe.2018.11.001.

Jeon, I. K., Kim, H. G., Jakhrani, S. H. & Ryou, J. S. 2021 Evaluation of the microstructure, mechanical, and durability properties of alkali-activated slag-based mortar with light-burnt dolomite powder. *J. Mater. Res. Technol.* **13**, 2220–2228. https://doi.org/10.1016/j.jmrt.2021.06.024.

Kang, L., Zhang, Y. J., Wang, L. L., Zhang, L., Zhang, K. & Liu, L. C. 2015 Alkali-activated steel slag-based mesoporous material as a new photocatalyst for degradation of dye from wastewater. *Integr. Ferroelectr.* **162**, 8–17. https://doi.org/10.1080/10584587.2015.1037197.

Khataee, A. R., Pons, M. N. & Zahraa, O. 2009 Photocatalytic degradation of three azo dyes using immobilized TiO_2 nanoparticles on glass plates activated by UV light irradiation: Influence of dye molecular structure. *J. Hazard. Mater.* **168**, 451–457. https://doi.org/10.1016/j.jhazmat.2009.02.052.

Ma, H., Zhu, H., Yi, C., Fan, J., Chen, H., Xu, X. & Wang, T. 2019 Preparation and reaction mechanism characterization of alkali-activated coal gangue-slag materials. *Materials (Basel)* **12**. https://doi.org/10.3390/ma12142250.

Mensah, K., Samy, M., Ezz, H., Elkady, M. & Shokry, H. 2022 Utilization of iron waste from steel industries in persulfate activation for effective degradation of dye solutions. *J. Environ. Manage.* **314**, 115108. https://doi.org/10.1016/j.jenvman.2022.115108.

Nasr, O., Mohamed, O., Al-Shirbini, A. S. & Abdel-Wahab, A. M. 2019 Photocatalytic degradation of acetaminophen over Ag, Au and Pt loaded TiO_2 using solar light. *J. Photochem. Photobiol. A Chem.* **374**, 185–193. https://doi.org/10.1016/j.jphotochem.2019.01.032.

Onen, N., Elkady, M., Elwardany, A., Fujii, M., Sekiguchi, H. & Shokry, H. 2023 Effective decontamination of methylene blue from aqueous solutions using novel nano-magnetic biochar from green pea peels. *Environ. Res.* **220**, 115272. https://doi.org/10.1016/j.envres.2023.115272.

Proctor, D. M., Fehling, K. A., Shay, E. C., Wittenborn, J. L., Green, J. J., Avent, C., Bigham, R. D., Connolly, M., Lee, B., Shepker, T. O. & Zak, M. A. 2000 Physical and chemical characteristics of blast furnace, basic oxygen furnace, and electric arc furnace steel industry slags. *Environ. Sci. Technol.* **34**, 1576–1582. https://doi.org/10.1021/es9906002.

Safo, K. & Berko, M. 2023 Novel immobilized titanium dioxide onto peanut shell-based activated carbon for advance oxidation process coupled with response surface models in organic wastewater treatment. *Engineering Proceedings* **37** (1), 1–7.

Safo, K., Noby, H., Matatoshi, M. & Naragino, H. 2022a Statistical optimization modeling of organic dye photodegradation process using slag nanocomposite. *Res. Chem. Intermed.* https://doi.org/10.1007/s11164-022-04807-5.

Safo, K., Noby, H., Matatoshi, M., Naragino, H. & El-Shazly, A. H. 2022b Solvothermal prepared slag nanocomposite as a catalyst for organic dye photodegradation. *Key Eng. Mater.* **931**, 125–130. https://doi.org/10.4028/p-u25360.

Safo, K., Noby, H., Mitsuhara, M., Naragino, H. & El-shazly, A. H. 2023 Environmental nanotechnology, monitoring & management H_2O_2 assisted steel slag nanocomposite for degradation of organic pollutant in an advanced oxidation process for suspension and spin-coated mode. *Environ. Nanotechnol. Monit. Manage.* **20**, 100836. https://doi.org/10.1016/j.enmm.2023.100836.

Samy, M., Ibrahim, M. G., Gar Alalm, M. & Fujii, M. 2020 Effective photocatalytic degradation of sulfamethazine by CNTs/LaVO4 in suspension and dip coating modes. *Sep. Purif. Technol.* **235**. https://doi.org/10.1016/j.seppur.2019.116138.

Sanad, M. M. S., Farahat, M. M., El-Hout, S. I. & El-Sheikh, S. M. 2021 Preparation and characterization of magnetic photocatalyst from the banded iron formation for effective photodegradation of methylene blue under UV and visible illumination. *J. Environ. Chem. Eng.* **9**, 105127. https://doi.org/10.1016/j.jece.2021.105127.

Sarkar, C., Basu, J. K. & Samanta, A. N. 2019 Synthesis of MIL-53(Fe)/SiO_2 composite from LD slag as a novel photo-catalyst for methylene blue degradation. *Chem. Eng. J.* **377**, 0–1. https://doi.org/10.1016/j.cej.2018.08.007.

Shi, H., Yang, S., Han, C., Niu, Z., Li, H., Huang, X. & Ma, J. 2019 Fabrication of Ag/Ag_3PO_4/WO_3 ternary nanoparticles as superior photocatalyst for phenol degradation under visible light irradiation. *Solid State Sci.* **96**, 105967. https://doi.org/10.1016/j.solidstatesciences.2019.105967.

Tetteh, E. K., Ezugbe, E. O., Asante-Sackey, D., Armah, E. K. & Rathilal, S. 2021 Response surface methodology: Photocatalytic degradation kinetics of basic blue 41 dye using activated carbon with TiO2. *Molecules* **26**. https://doi.org/10.3390/molecules26041068.

Tossavainen, M., Engstrom, F., Yang, Q., Menad, N., Lidstrom Larsson, M. & Bjorkman, B. 2007 Characteristics of steel slag under different cooling conditions. *Waste Manage.* **27**, 1335–1344. https://doi.org/10.1016/j.wasman.2006.08.002.

Tsakiridis, P. E., Papadimitriou, G. D., Tsivilis, S. & Koroneos, C. 2008 Utilization of steel slag for Portland cement clinker production. *J. Hazard. Mater.* **152**, 805–811. https://doi.org/10.1016/j.jhazmat.2007.07.093.

Vaiano, V., Sacco, O. & Matarangolo, M. 2018 Photocatalytic degradation of paracetamol under UV irradiation using TiO_2-graphite composites. *Catal. Today* **315**, 230–236. https://doi.org/10.1016/j.cattod.2018.02.002.

Villota, N., Lomas, J. M. & Camarero, L. M. 2016 Study of the paracetamol degradation pathway that generates color and turbidity in oxidized wastewaters by photo-Fenton technology. *J. Photochem. Photobiol. A Chem.* **329**, 113–119. https://doi.org/10.1016/j.jphotochem.2016.06.024.

Wang, Z., Qi, J., Feng, Y., Li, K. & Li, X. 2014 Preparation of catalytic particle electrodes from steel slag and its performance in a three-dimensional electrochemical oxidation system. *J. Ind. Eng. Chem.* **20**, 3672–3677. https://doi.org/10.1016/j.jiec.2013.12.065.

Xu, Y., Liu, J., Xie, M., Jing, L., Xu, H., She, X., Li, H. & Xie, J. 2019 Construction of novel CNT/$LaVO_4$ nanostructures for efficient antibiotic photodegradation. *Chem. Eng. J.* **357**, 487–497. https://doi.org/10.1016/j.cej.2018.09.098.

Yang, Y., Wang, P., Shi, S. & Liu, Y. 2009 Microwave enhanced Fenton-like process for the treatment of high concentration pharmaceutical wastewater. *J. Hazard. Mater.* **168**, 238–245. https://doi.org/10.1016/j.jhazmat.2009.02.038.

Yanyan, L., Kurniawan, T. A., Ying, Z., Albadarin, A. B. & Walker, G. 2017 Enhanced photocatalytic degradation of acetaminophen from wastewater using WO_3/TiO_2/SiO_2 composite under UV–VIS irradiation. *J. Mol. Liq.* **243**, 761–770. https://doi.org/10.1016/j.molliq.2017.08.092.

Zia, J. & Riaz, U. 2020 Microwave-assisted degradation of paracetamol drug using polythiophene-sensitized Ag-Ag_2O heterogeneous photocatalyst derived from plant extract. *ACS Omega* **5**, 16386–16394. https://doi.org/10.1021/acsomega.0c00405.

First received 23 May 2023; accepted in revised form 12 September 2023. Available online 4 October 2023